HHS Public Access

Author manuscript

Mater Sci Eng C Mater Biol Appl. Author manuscript; available in PMC 2019 March 01.

Published in final edited form as:

Mater Sci Eng C Mater Biol Appl. 2018 March 01; 84: 67–79. doi:10.1016/j.msec.2017.11.021.

Novel high-strength, low-alloys Zn-Mg (<0.1 wt% Mg) and their arterial biodegradation

Hualan Jin[a,b], **Shan Zhao**[a], **Roger Guillory**[c], **Patrick K. Bowen**[a,d], **Zhiyong Yin**[a], **Adam Griebel**[e], **Jeremy Schaffer**[e], **Elisha J. Earley**[c], **Jeremy Goldman**[c], and **Jaroslaw W. Drelich**[a,*]

[a]Department of Materials Science and Engineering, Michigan Technological University, Houghton, MI 49931,USA

[b]School of Materials Science and Engineering, Nanchang University, Nanchang 330031, People Republic of China

[c]Department of Biomedical Engineering, Michigan Technological University, Houghton, MI 49931, USA

[d]Research & Development, Deringer-Ney Inc., Bloomfield, CT 06002

[e]Research & Development, Fort Wayne Metals, Fort Wayne, IN 46809

Abstract

It is still an open challenge to find a biodegradable metallic material exhibiting sufficient mechanical properties and degradation behavior to serve as an arterial stent. In this study, Zn-Mg alloys of 0.002 (Zn-002Mg), 0.005 (Zn-005Mg) and 0.08 wt% Mg (Zn-08Mg) content were cast, extruded and drawn to 0.25 mm diameter, and evaluated as potential biodegradable stent materials. Structural analysis confirmed formation of Mg_2Zn_{11} intermetallic in all three alloys with the average grain size decreasing with increasing Mg content. Tensile testing, fractography analysis and micro hardness measurements showed the best integration of strength, ductility and hardness for the Zn-08Mg alloy. Yield strength, tensile strength, and elongation to failure values of >200–300 MPa, >300–400 MPa, and >30% respectively, were recorded for Zn-08Mg. This metal appears to be the first formulated biodegradable material that satisfies benchmark values desirable for endovascular stenting. Unfortunately, the alloy reveals signs of age hardening and strain rate sensitivity, which need to be addressed before using this metal for stenting. The explants of Zn-08Mg alloy residing in the abdominal aorta of adult male Sprague-Dawley rats for 1.5, 3, 4.5, 6 and 11 months demonstrated similar, yet slightly elevated inflammation and neointimal activation for the alloy relative to what was recently reported for pure zinc.

Keywords

Zn-Mg alloys; endovascular stent; degradability; properties

*Corresponding author: Jaroslaw Drelich, Phone: 1-(906)487-2932; jwdrelic@mtu.edu.

1 Introduction

Arterial disease is detrimental to the continuous blood flow in arteries. Due to many well-documented benefits, endovascular scaffolds are commonly deployed on balloons using angioplasty procedures to restore and sustain blood flow through diseased blood vessels [1, 2]. However, long term complications such as chronic inflammation [3], late-stage thrombosis [4], and stent corrosion and fracturing [5] can overshadow the short term benefits. Moreover, arterial restenosis caused by neointimal proliferation is commonly encountered in traditional stent implantations [6, 7].

Biodegradable stents would eliminate much of the long term health risks and complications associated with the use of current permanent and drug-eluting stents [8]. Generally, they would retain their mechanical characteristics and structural integrity for about six months before being decomposed, metabolized, and excreted by the body, leaving behind a renewed vessel segment and removing the sources of inflammation or thrombosis [9]. In more than twenty years of research on biodegradable materials for endovascular stent applications, two classes of materials, polymers and metals, have been widely tested. Development of polymeric stents progressed at a higher pace than metallic ones due to availability of polymers of proven biocompatibility. For example, poly-L-lactic (PLLA) has been proven to have a satisfactory biocompatibility [10]. However, because the biodegradable polymers have low ultimate tensile strength, typically in a range of 36–45 MPa, the polymeric stents rely on struts of larger dimensions (strut thickness can vary from 150 to 300 μm) than metallic stents [11]. This characteristic contributes to the similar restenosis rates that have been reported between polymeric scaffolds and earlier generation bare metal stents [12]. Other shortcomings shown in polymeric stents include their inability to enlarge fully during balloon expansion [13].

Biodegradable metals have received much attention in recent years. Having superior mechanical properties as compared to polymers, metals could provide a more ideal platform as interim implants if their biocompatibility is close to or better than biodegradable polymers [14]. In the selection of elements for biodegradable metals, elements with biological roles in the human body are often considered first. For example, both iron (Fe) and magnesium (Mg) are essential elements of our body and have been tested as bioabsorbable implants in the last several years [15–21]. As a result, both Fe and Mg can serve as base metals for manufacturing strong scaffolds, desirable in widening the diseased blood vessel and providing support during the healing period. Fe and Mg and their alloys have a tensile strength and elastic modulus that are superior to those of biodegradable polymers [22, 23]. Moreover, a metal's mechanical characteristics make stent manufacturing advantageous relative to polymers. In addition, the favorable mechanical properties of metals allow for cutting stents with small diameter struts, desirable in combating the restenosis rate [24]. Mg and its alloys have a unique advantage of eliciting low thrombosis [25], which is believed to explain the lack of thrombotic complications in past clinical studies [9]. However, commercial purity Mg has a high degradation rate along with an associated and potentially harmful release of hydrogen gas. Some studies have reported that Mg completely dissolves after implantation in 60–90 days [26, 27], not enough for endovascular stent applications. On the contrary, although Fe possesses excellent biocompatibility without systemic iron

toxicity, its slow degradation [28] along with the formation of voluminous corrosion products precludes this metal from biomedical applications requiring absorbable implants with substantial volume or section thickness [24, 29]. Various alloying and coating strategies are being pursued in each of these classes to address their shortcomings, with mixed success [30–38].

Research attention has shifted in the last few years to alternative metals such as Zn [23, 39–42]. The standard corrosion potential of Zn is −0.8 V, which is between Fe (−0.4 V) and Mg (−2.4 V) [43], making this metal electrochemically more noble than Mg and more active than Fe. Moreover, Zn is an indispensable element for human health and is the second most abundant transition metal element in the human body. It is also a very important element for cell proliferation, as well as the functioning of both the immune and nervous systems [44, 45].

Observations from pure Zn wires implanted into the rat abdominal aorta for up to 6 months has been reported by Bowen et al. [39, 46]. During the first 3 months, the penetration rate for pure Zn remained below 0.02 mm/yr, but the corrosion rate doubled at 4.5 and 6 months. The study also revealed that zinc oxide and zinc carbonate were the primary corrosion products during *in vivo* metal degradation, and that arterial tissue regenerated within the original footprint of the implant during degradation. More importantly, it was shown that Zn could inhibit arterial restenosis after device implantation because of its suppressive effect against arterial smooth muscle cells [46].

Although pure Zn appears to be biocompatible in the endovascular environment with a nearly ideal corrosion rate, its strength needs to be enhanced for vascular stent applications [39, 42]. By adding alloying elements and/or thermos-mechanical refinement of the microstructure, improvements in the mechanical properties of pure Zn can be accomplished [14]. Among many candidates, the Zn-Mg binary alloys are expected to achieve the mechanical strength and biocompatibility required for bioabsorbable stent applications; although a concomitant drop in its ductility reported in previous studies to less than 5–10% [47–53] is not acceptable for stent applications.

In this study, we explored the feasibility of Zn-Mg alloys for endovascular stent applications. The use of Mg in this binary alloy was motivated by the excellent biocompatibility of Mg. Previous reports also suggest an improvement in the strength of Zn metals alloyed with Mg [40, 52, 53]. However, in contrast to previous studies on these alloys [54–57], the content of Mg in formulated Zn-Mg alloys was selected to be substantially below 1 wt%. By reducing the content of Mg in the Zn-Mg alloy, we intended to preserve a high ductility of the Zn alloys, a critical feature in endovascular stent applications. In this paper, we describe our findings regarding the microstructure, mechanical properties, and *in vivo* corrosion behavior of Zn-0.002, −0.005, and −0.08 wt.% Mg alloys.

2. Selection of Alloys

The Zn-Mg phase diagram for Mg content not exceeding 20 wt% is shown in Figure 1a. Figure 1b shows a portion of Figure 1a for Mg content from 0 to 0.2 wt% [58], which

includes all alloy compositions of interest. These phase diagrams indicate that the solid solubility of Mg in Zn is very low and the Mg_2Zn_{11} intermetallic phase precipitates with little Mg addition. When cooling down Zn-Mg metal liquid to about 419 °C, a primary Zn phase forms first. After cooling down to 364 °C, a eutectic microconstituent containing Zn and Mg_2Zn_{11} forms along the grain boundaries of primary Zn grains [52, 55, 59–61]. The solubility of Mg in a Zn matrix seems to be an open question [58]. Figure 1b indicates moderate solubility of ~0.15 wt.% of Mg in Zn at the eutectic temperature. Other system reviews [62, 63] indicate different or negligible solubility, with the latter group treating the eutectic reaction as a simple decomposition from the liquid to pure Zn and Mg_2Zn_{11}. This is notable, as systems of the former configuration may exhibit limited age hardenability, whereas the latter may only be wrought hardened.

The introduction of Mg_2Zn_{11} intermetallic phases can provide a hardening effect in Zn-Mg alloys via dispersion strengthening [56, 59], important to increasing the strength of the material relative to pure zinc. However, high Mg contents can result in brittle materials with reduced plasticity, as reported by others for the as-cast alloys [42, 56, 59]. To avoid an excessive drop in ductility, Mg contents below 0.1 wt% were selected in this study.

3. Experimental

3.1 Zn and Zn-Mg alloys

Zn wire from Goodfellow (99.99+% purity) with a diameter of 0.25 mm was used as a reference material in this study. The Zn-Mg alloys were cast at Michigan Tech and reduced to 0.25 mm wires at Fort Wayne Metals as described below.

Three different Zn-Mg alloys were prepared including Zn-0.08 wt% Mg, Zn-0.005 wt% Mg and Zn-0.002 wt% Mg, which are marked as Zn-08Mg, Zn-005Mg, and Zn-002Mg, respectively, throughout this contribution. The alloys were cast in-house using a vacuum induction casting apparatus per the following procedure.

A 304 stainless steel (304 SS) mold and a fine-grained graphite crucible were cleaned from previous melts prior to melting by etching with *ca.* 6N HCl, thoroughly rinsed with deionized water, and baked at 110°C overnight. Pure reagents-99.99% Zn (Alfa Aesear) 10 × 2 mm round “splat shot” and 99.99% Mg turnings-were weighed, mixed, and added to the graphite crucible. The crucible and mold were placed in the appropriate positions and aligned. The chamber was evacuated to 15–25 mTorr under rough vacuum, then to 200–250 μTorr under high (diffusion pump) vacuum, and then backfilled with high-grade (99.998%) Ar to 684 Torr. Melting was conducted at 2.5–3 kW input power for 10–15 min, and the melt was poured at a 510°C pyrometer readout-likely closer to 470°C real melt temperature-using an auto-pour routine. After allowing the melt to cool for 10 min, the chamber was evacuated to < 100 mTorr, and the ingot was allowed to cool further for 1 h. The chamber was then vented to atmosphere, the ingot was removed and quenched to 15°C under running water.

The ingots obtained with a diameter of ~50 mm and a height of ~60 mm were then extruded at 150 °C to a diameter of 13 mm. The extruded rods of 13 mm in diameter were centerless

ground to provide a pristine surface finish and were then drawn into wires of 0.25 mm in diameter by Fort Wayne Metals (Fort Wayne, IN).

The elemental composition of the Zn-Mg alloy wires was determined by Inductively Coupled Plasma Optical Emission Spectrometry (ICP-OES) (PerkinElmer Optima 7000DV, Waltham, MA). About 80 mg of each respective alloy wire was dissolved in 10 ml of 6M HCl, which was diluted for ICP-OES analysis.

3.2 Microstructure characterization

Longitudinal and transverse samples of each alloy were mounted in low viscosity epoxy, which was allowed to set for at least 24 hours. The samples were ground on 600-grit and 800-grit SiC paper, and then were polished using 6 μm, 1 μm diamond paste, and a 0.05 μm Al_2O_3 suspension. The samples were etched in a solution consisting of 6 g picric acid, 5 ml acetic acid, and 10 ml water and 100 ml ethanol. The microstructure of samples was imaged using a Leica EC3 (Leica Microsystems; Buffalo Grove, Illinois) digital camera on an Olympus PMG-3 optical microscope (Olympus, Shinjuku, Tokyo, Japan).

An XDS 2000 θ/θ X-ray diffractometer (Scintag Inc., Cupertino, CA) with CuKα radiation (k = 1.540562 Å) was utilized in detecting X-ray diffraction (XRD) of the Zn alloys. The fast scans were performed between 10° to 90° in the 2θ range with a scan speed of 0.5°/min and a step size of 0.02°. The slow scans were performed between 31° to 49° in the 2θ range with a scan speed of 0.1°/min and a step size of 0.02°. The glass slide was covered with conductive tape on top and the eight 10 mm-long wires were laid down and stacked together on the tape.

3.3 Mechanical properties

The tensile test samples are shown in Figure 2a. The end sections (~5 mm) of the Zn-Mg wires were rough ground using 120 grit SiC sandpaper prior to mounting, which could improve their bonding to the epoxy and prevent sample pullout.

Tensile tests were carried out using a Bose ELF 3200 mechanical tester (Bose Inc., MN, US) equipped with a 22.2 N load cell. The wires were stored for 2–3 hours (0 day), 1 day, 9 days, half year, and one year at room temperature, before the test. Bent wires were mounted on two polycarbonate (PC) holders (about 30 mm wide, 40 mm long) using Loctite General Purpose epoxy (Henkel Corporation; Westlake, OH). The two PC holders were placed 10 mm apart to allow for a gauge section of that size (Figure 2a). Two toothpicks taped to them were used to maintain the stability and distance between the PC holders while the tested wire was mounted between the toothpicks. After curing, the samples were fastened by the grips and the toothpicks were removed (Figure 2b). Tests were performed using strain rates of 1.67×10^{-4} s^{-1}, 10^{-3} s^{-1}, 3.3×10^{-3} s^{-1} and 1.67×10^{-2} s^{-1} until fracture. Yield strength, tensile strength and percent elongation to fracture were calculated from the stress-strain curves. The standard error was calculated from six samples per measurement.

The fracture surfaces were examined under SEM after tensile testing. The measure of ductility was the reduction of area, given by (1).

$$\text{Reduction of area} = \frac{(A_0 - A_f)}{A_0} \times 100 \quad (1)$$

where A_o and A_f are the original and final (fracture) cross-sectional areas, respectively, of the test specimen.

Vickers micro-hardness (HV) tests were made at a 200 g load using an M-400-G1 digital hardness tester (LECO, St Joseph, MI) at a fixed dwell time of 10 s. Sixteen indentations were made on a longitudinal section of pure Zn and each Zn-Mg wire, in the area of wire axis. A standard error was calculated from the sixteen different points.

3.4 In vivo study and explant characterization

The Zn-Mg wire samples (which were stored for 3 to 5 weeks) were cut into 15 mm segments and the ends smoothed to remove any burrs (for arterial wall implantation) or sharpened (for puncture into the arterial lumen). Prior to implantation, the Zn-Mg wires were cleaned using a ProCleaner TM cleaning device (BioForce Nanosciences; Ames, IA) for 30 minutes to remove dust or other loose contaminants and sterilize the surface.

Adult male Sprague-Dawley rats were used for *in vivo* evaluation. All animal tests were permitted by the animal care and use committee (IACUC) of Michigan Technological University. The 15 mm wires were either advanced within the lumen (for latter biocompatibility evaluation by histological analysis) or wall (for metallographic analysis and determination of corrosion behavior) of the abdominal aorta of adult male Sprague-Dawley rats. Thus, the Zn-Mg wires were either immersed in the flowing blood to simulate the initial environment of a stent or placed within the arterial extracellular matrix to simulate the long term encapsulated state of a stent. After a period of 1.5, 3, 4.5, 6 and 11 months, the rats were euthanized and rat aortas with the implanted wires were explanted. To protect any corrosion layer on the wires' surfaces, the wires were immersed in absolute ethanol for a short time. All samples were preserved in a low humidity atmosphere before analysis.

In order to determine the cross sectional area (CSA) reduction and the penetration rate of the Zn-Mg alloys after degradation in the aortas of rats, the explants were mounted in epoxy, inside a silicone tube with diameter of 12.5 mm. After curing, the mounted wire was removed from the silicone tube and then cut transversely into 16–20 slices having thickness of about 1 mm. The cross-sectioned slices were then mounted in epoxy again. After curing, mounted slices were ground with 600-grit and 800-grit SiC, polished with 6 μm and then 1 μm diamond paste, and finished with 0.05 μm Al_2O_3 suspensions. The polished cross-sections were coated with carbon to improve conductivity before imaging with a JSM 6400 scanning electron microscope (SEM) (JEOL, Peabody, MA). The images were taken using its backscattered electron detector at 15 kV accelerating voltage and a working distance of 39 mm.

The cross sectional area (CSA) of the obtained backscattered electron images of corroded wires was analyzed using ImageJ software [64]. Example of cross section of a corroded wire

with marked metallic section (red area) and surrounding corrosion product (outside the red area but inside of the circle) is shown in Figure 3. The selection of metallic area (marked as red area A) was done by selecting the brightest pixels by thresholding. The perimeter of original wire, and associated cross-sectional area, was approximated by a circle/ellipse (yellow B). Based on the cross-sectional area measurement, a penetration rate was calculated for each sample. The change in CSA was used to find the penetration rate at each section using equation (2) [65]:

$$p = \frac{\sqrt{\frac{A_0}{\pi}} - \sqrt{\frac{A_t}{\pi}}}{t} \quad (2)$$

where p and t are the penetration rate and the in vivo implantation time, respectively. A_0 is the nominal CSA and A_t is the CSA at time point t.

On average 18 (±2) images were produced for each specimen. Both mean values and standard error are reported.

3.5 Histological evaluation

Selected sections of wires with aortas were snap-frozen in liquid nitrogen and cryo-sectioned for histological analysis. Before staining, samples were preserved in a −80 °C freezer. Frozen samples were cross-sectioned at a 10 μm thickness with a Thermo-Scientific HM 550 P cryostat. Tissue sections were then placed on warm VWR Histobond slides and fixed in −20°C absolute ethanol for 60 s and washed three times in PBS (Sigma Aldrich) for 5 min before staining commenced. Gills-3 hematoxylin solution was pipetted onto each slide for 2–5 min, or until over-stained (determined by visual examination). Slides were then dipped in a 900 mL bath of distilled water that had been acidified to pH = 1.8–2.0 by adding HCl. After 5 dips in the acidic bath, the samples were rinsed in distilled water for 1–5 min. Slides were then washed twice with 95% ethanol (v/v). The slides were counterstained with Eosin Y working solution (0.25%), which was micro-pipetted onto each slide for 45 s. Immediately after counterstaining, the slides were rinsed and dehydrated in two changes of absolute ethanol for 5 min apiece. The slides were then cleared twice with xylene substitute for 5 min, and mounted under a cover slip using Eukitt mounting medium. Samples were imaged using an Olympus BX51, DP70 bright-field microscope (Upper Saucon Township, PA).

4. Results

The compositions of the Zn-Mg alloys formulated in this study as analyzed using an ICP method are given in Table 1. The content of Mg was 0.002 wt%, 0.005 wt%, and 0.08 wt% and other elements including Al, Cd, Cu, Fe, Ni and Pb were detected as trace impurities in the formulated Zn-Mg alloys.

4.1 Microstructure characterization

The optical micrographs for the Zn-Mg alloys are shown in Figure 4. Coarse grains with an average diameter of ~76 μm were observed in the Zn-002Mg alloy. With increasing Mg content, grain refinement of the Zn-Mg alloys was achieved. The grain size was reduced by one order of magnitude when the content of Mg was increased to 0.005 and 0.08 wt%. The Zn-005Mg and Zn-08Mg alloys had ~7 and ~6 μm grains on average, respectively (Table 2).

Based on the Mg-Zn phase diagram presented in Section 2 [66], it is predicted that all three different Zn-Mg alloys consist of primary α-Zn and Mg_2Zn_{11}. Figure 5 shows the XRD patterns of the Zn-08Mg alloy. These XRD patterns confirm the presence of both α-Zn and Mg_2Zn_{11} phases, in accordance with an earlier report on Zn-Mg alloys [56]. Increasing Mg content in the Zn-Mg alloys generally lead to the formation of larger quantities of Mg_2Zn_{11}.

4.2 Mechanical properties

4.2.1 Tensile testing and hardness measurements—Table 3 lists the tensile and hardness test results for the three Zn-Mg wires of different shelf time. Because the majority of tests and characterization on formulated wires reported in this contribution were carried out on specimens stored for half a year, we start discussion with the set of results for these samples.

The Vickers hardness values for the three Zn-Mg wires are shown in Table 3. The Zn-002Mg had the lowest hardness value of 45 HV, nearly identical to Zn (42 HV). The Zn-08Mg alloy had the highest average hardness of 103 HV. Increasing hardness correlates well with increasing Mg content, associated reduction in grain sizes.

As shown in Table 3, the Zn-002Mg alloy had the lowest yield strength, tensile strength, and elongation among all three alloys. The yield strength, tensile strength and percent elongation for the Zn-Mg alloys increased with the increasing Mg content.

Figures 6 and 7 showed the representative tensile stress-strain curves of Zn-08Mg wires. Figure 6a shows the representative tensile stress-strain curves for Zn-08Mg wires with different storage times, which were recorded at a strain rate of 0.0033/s. The curves reveal age hardening of this alloy. The tensile strength of nearly 270 MPa recorded a few hours after wire drawing increased to nearly 500 MPa after ~ 24 hours and 9 days. Elongation of 30% dropped to 20% and 13% in the same time of storage sequence. After one year of storage the wire tensile strength dropped by only ~10%. Elongation unfortunately dropped to less than 4%.

The same Zn-08Mg wire also showed strain rate sensitivity during tensile testing. Figure 6b shows examples of tensile testing results for the wire left on a shelf for 9 days. Three stress-strain curves show increases in tensile strength of the Zn-08Mg wire from ~230 MPa, to ~500 MPa, and to >600 MPa as the strain rate increases from 0.000167 to 0.0033 and 0.033/s, respectively. The elongation value dropped from ~90% to ~13% and ~2.3% over the same sequence of strain rate tensile testing conditions. Samples stored for one year showed a similar strain rate sensitivity (Figure 7). Tensile testing at 0.001/s and 0.0033/s strain rates

revealed a drop in elongation from >30% to ~5%, with tensile strength increasing from ~370 MPa to ~430 MPa (Figure 7b).

4.2.2 Fracture surface—The fracture surfaces of the tensile samples of the Zn-Mg alloys (storage half a year, strain rate $1.00\times10^{-3}s^{-1}$) are shown in Figure 8. The Zn-002Mg alloy exhibited a brittle fracture, but the fracture surfaces of Zn-005Mg and Zn-08Mg alloys had characteristic dimples, and showed a more ductile fracture surface. Also, the diameter of the wire specimens systematically decreased around the fractured surface with an increasing content of Mg, suggesting an increasing ductility.

Figure 9 shows the fractured surfaces of the tensile samples for Zn-005Mg and Zn-08Mg alloys. As shown by these two micrographs, the percent reduction in cross-sectional area as the result of elongation and fracture was ~63% and ~82% for these two Zn-Mg alloys, respectively. A change took place in the fracture behavior of the Zn-Mg alloys as the Mg content increased, and the Zn-08Mg alloy showed a more ductile behavior than Zn-005Mg. A close look into the micrographs revealed that the ductile fracture generally took place along planes (where the shear stress is at a maximum).

4.3 In vivo biocorrosion

Representative backscattered electron images of cross sections for explants retrieved after 1.5, 3, 4.5, 6 and 11 months from the abdominal aorta of a Sprague-Dawley rat are shown in Figure 10. The intact Zn-Mg alloys are visible as a bright feature in the center, surrounded by corrosion product, artery tissue, and epoxy. The remaining metallic cores of these explants had irregular edges, caused by a partial degradation of implanted wires. As implantation time progressed, the remaining metallic area became smaller and more irregular.

Image analysis of the sample sections enabled measurement of cross sectional area reduction and average penetration rates, as presented in Figure 11 and 12, respectively. Penetration rate analysis showed the degradation rates of Zn-002Mg and Zn-005Mg at 1.5 months were ~0.029 mm/y and 0.021 mm/y, respectively, which are above the values recorded for pure Zn but near the benchmark value proposed for ideal endovascular stent degradation (0.02 mm/y) [67]. After 3 months, their degradation rates reduced to below what was observed for pure Zn. Overall, the degradation rates of Zn-002Mg and Zn-005Mg were close and slightly lower than what we reported for pure Zn [39], but above the ideal degradation benchmark (0.02 mm/y). The degradation rate of Zn-08Mg was 0.012–0.015 mm/y at 1.5–4.5 months, below the benchmark value of 0.02 mm/y at 1.5–4.5 months. However, the degradation rate of Zn-08Mg increased to 0.027 mm/y and 0.023 mm/y at 6 and 11 months, respectively. This degradation acceleration in later stages is viewed as a favorable feature of degradable implants because the stent should dissolve in the body as soon as possible after fulfilling its mission as mechanical support during the healing process. It should be noted that biocorrosion of Zn-Mg alloys progressed quite uniformly, as reflected in the standard error bars shown in Figures 11 and 12.

4.4 In vivo biocompatibility analysis

The biocompatibility of the Zn-Mg alloys was assessed by examining histological images from luminally implanted wires, with representative 6 and 11 month implantation images shown in Figure 13 and 14, respectively. The biological host response to the three magnesium concentrations was generally similar to what we recently reported for pure zinc [46], although with a slightly higher presence of inflammatory cell infiltrates which lead in some cases to a slightly greater degree of neointimal activation or arterial constriction. At 6 months, intimal activation can be seen from the media layer of the Zn-002Mg progressing away from the implant site and protruding into the lumen (guided by the red bars). At Zn-005Mg, a non-stable neo-intima had formed (guided by the blue bar), along with native intimal activation (depicted by the red bar). Although the Zn-08Mg does not show distinct intimal thickening, it does exhibit a modest degree of chronic inflammation (shown by the red asterisks), and a decrease in luminal cross sectional area. At 11 months in vivo, relatively low cell density can be seen around the base the Zn-002Mg with a stable neointimal endothelium. The Zn-005Mg elicited chronic inflammation in the wall of the artery (identified by the red asterisks). Unlike the Zn-002Mg, the Zn-005Mg experienced an unorganized intimal growth, lacking a confluent endothelial cell layer (shown by the red arrows). The Zn-08Mg experienced intimal thickening (shown by the red bar), accompanied by a discontinuous endothelium (shown by the red arrows). The degree of inflammation for Zn-08Mg appears to subside from 6 to 11 months. Some degree of cell toxicity is evident in both the Zn-005Mg and the Zn-08Mg as evidenced by the appearance of dense cell regions. In summary, there appears to be a trend of slightly worsening biocompatibility with increasing Mg content. In contrast, the neointima that formed around pure zinc implants was generally restricted to the implant vicinity and arterial constriction was not detected [46]. Of note, the luminal narrowing effects are acceptable from an application standpoint, as the presence of mechanical scaffolding would be expected to counteract this tendency.

5 Discussion

5.1 Structural and mechanical characteristics of alloys

By varying the content of Mg, the microstructure and mechanical properties of Zn-Mg alloys were manipulated in this study. It was observed that the Zn-002Mg alloy had very coarse grains, averaging around 76 μm in diameter (Figure 4a), and this alloy consisted of primary dendrite-type grains and eutectic mixtures. Due to the extrusion process at 150°C, the Zn matrix may experience dynamic and static recrystallization and growth, which produces coarse grains. This grain growth could be hindered by more additions of Mg (shown in Figure 4b,c), since the growth speed is determined by the different activation energy for grain boundary motions [68, 69]. Adding Mg above 0.002% produced a significantly refined structure after extrusion and drawing. The Zn-08Mg alloy had very small grains, averaging about 6 μm in diameter (Table 2).

According to the Mg-Zn phase diagram (Figure 1) [66], the microstructure of Zn-Mg alloys should consist of primary α-Zn grains and a Mg_2Zn_{11} intermetallic. The XRD results shown in Figure 5 confirmed the presence of these two phases with characteristic peaks on the XRD pattern for the zinc phase at 36.4°, 43.24°, 54.36°, 70.14 °, 77.13 ° and 82.4 °and

Mg_2Zn_{11} phase at 32.6°, 34.8 ° and 44.8°. When increasing Mg from 0.0002 and 0.005% to 0.08%, the content of Mg_2Zn_{11} increased. The "microsegregation" phenomenon could have occurred due to the excess Mg_2Zn_{11} in solid solution of Zn matrix, and is responsible for structural strengthening. The concentration of Mg_2Zn_{11} in the wire center of Zn-08Mg as can be interpreted from micrograph in Figure 4c could be due to the cooling process where the excess Mg was unable to go into α-Zn grains near the surface and was forced to migrate to the center. These second phase particles exhibited a preferred wire-axial orientation, produced during extrusion and drawing. The elongated intermetallics are commonly known as stringers in other materials [70, 71].

As shown by the phase diagram in Figure 1, the Mg_2Zn_{11}strengthening phase precipitates from the liquid when below the melting point. The resulting Zn matrix and precipitated phase formed a hypoeutectic structure. The grain size decreased from 76 to 6 microns with increasing Mg content in Zn-Mg alloys from 0.002 to 0.08 wt% (Table 2). A drastic reduction in grain sizes had a significant impact on the strength and hardness of the alloys (Table 3).

For Zn-08Mg (stored for half a year), TYS and UTS were 221 ± 14 and 339 ± 42 MPa, respectively, with elongation to failure ~40%. Surprisingly, the ductility of the wires increased with increasing Mg content, as reflected by the necking of wires during fracturing (Figures 8 and 9). This could be due to the finer grain size with increasing Mg content.

The mechanical properties for all the Zn-Mg alloys studied in the past are compiled in Table 4. As shown by these data, hot-extrusion improves the strength of Zn-Mg alloys as compared to as-cast Zn-Mg materials with the same Mg content. In the as-cast state, the structural compositions of this alloy rely primarily on Zn dendrites and the Zn + Mg_2Zn_{11} interdendritic eutectic network [42]. After hot extrusion, eutectic regions become oriented in the extrusion direction and the grains are usually refined and become more homogeneous, with reduced area fraction of the eutectic mixture [54].

Mostaed et al. [52] characterized Zn-0.15Mg, Zn-0.5Mg, Zn-3Mg alloys after two-stage hot-extrusion at 250 °C (with an extruded ratio of 6:1 to obtain cylindrical rods) and 300 °C (with an extruded ratio of 16:1 to obtain small tubes.) The data showed that both TYS and UTS consistently increase with increasing Mg content, with a final product achieving values of approximately 290 and 400 MPa, respectively, for Zn-3Mg. Unfortunately, elongation to fracture dropped from 60% to 0.8%. Kubasek et al. [53] researched the hot-extruded Zn-0.8Mg at 300 °C (with ratio of 10:1 and rate of 2 mm/min). They report TYS and UTS values of around 200 and 300 MPa, respectively, for this alloy. The Zn-0.8Mg alloy retained relatively good plasticity with an elongation to fracture value of 15% attributed to a lack of networked intermetallic phases. Gong et al. [40] studied the hot-extruded Zn-1.0Mg alloy (extrusion temperature = 200 °C, ram rate = 20 mm/s, extrusion ratio = 16), and the values for TYS and UTS reported are 180 MPa and 252 MPa, respectively, with an elongation to fracture of 13%. Vojtech et al. [56] prepared the Zn-1.6Mg alloys by hot-extrusion at 300 °C with an extrusion rate of 2 mm/min and a ratio of 10:1. The extruded Zn-Mg alloy exhibited good TYS and UTS (~290 and ~360 MPa, respectively), but a low elongation of 6%.

None of the previous reports suggested any instabilities of Zn-Mg alloys and neither age hardening nor strain rate sensitivity were studied. Figure 6a shows representative tensile stress-strain curve for Zn-08Mg wires shelved over different times. It shows that tensile strength increases and elongation to fracture value decreases with increasing storage time. Figure 6b and Figure 7b show example stress-strain curves produced at different strain rates. The results clearly show decreases in elongation to failure when the Zn-08Mg wire is tested under tensile load at increasing strain rate. In summary, the Zn-08Mg alloy exhibited significant shelf-aging and strain-rate sensitivity phenomenon despite favorable mechanical characteristic.

The natural aging phenomenon observed for low Mg content Zn-Mg alloys is likely a result of formation and then migration of the precipitate phase (Mg_2Zn_{11}) to grain boundaries. The phase diagram in Figure 1 indicates a very low solid solubility of Mg in Zn. The Mg_2Zn_{11} intermetallic phase precipitates with little Mg addition. When the Zn-Mg alloy is cooled down to about 419 °C, the Zn phase nucleates first. After cooling down to 364 °C, the Mg_2Zn_{11} intermetallic phase precipitates. The final product is eutectic containing Zn and Mg_2Zn_{11} formed along the grain boundaries of primary Zn and some Mg_2Zn_{11} freely precipitated inside the grains. Over time, Mg_2Zn_{11} inside the grains continues to precipitate and migrate to grain boundaries. This results in Mg_2Zn_{11} phase enrichment zones and the age-hardening phenomenon.

During the tensile test, dynamic recrystallization is likely to occur because the recrystallization temperature is 10 °C for pure Zn [72]. The dynamic recrystallization process is related to rate of deformation, and the increased strain rate makes the plastic deformation harder, which leads to the insufficient development of dislocation movement and little ductility of the Zn-Mg alloys [73, 74]. The strain rate sensitivity of Zn-Mg alloys is also likely related to the mobility of dislocations. The increasing strain rate and ensuing movement of dislocations under the external force will result in plastic deformation of the Zn-Mg alloy. The slip of a dislocation has a certain speed, that is to say the slip process needs some time. In general, higher strain rate leads to higher dislocation density, greater tensile strength, and less ductility of the Zn-Mg alloys (Figure 7b) [75, 76].

Both metal strength and ductility are sensitive to grain sizes, according to the Hall-Petch relation [77], where finer grains result in higher grain boundary strengthening. The same rule is also generally true for Zn and its alloys, although there is not enough experimental data to draw more specific correlations. The grain sizes of the studied Zn-Mg alloys become more homogeneous and fine with increasing Mg content, which leads to the enhancement of strength for Zn-Mg alloys (studied herein and in other laboratories; Table 4). However, the trend of elongation to failure was different for the three alloys studied herein. The elongation to fracture values increase from about 17% to 40% when increasing the Mg content from 0.002 wt% to 0.08 wt % (Table 4). We attribute this to an excessively large grain size in the Zn-002Mg wire which leads to non-uniform deformation and quicker localization of strain.

Further, since a radially expanded stent must undergo a significant plastic deformation when expanded into its working state, it should be made of a material having a low yield point, high tensile strength and sufficient strain hardening rate to avoid strain localization. The lack

of strain-hardening observed in tensile testing of Zn-Mg alloys is a challenge to overcome in future work.

5.2 Biocompatibility of alloys

The increase in the concentration of Mg_2Zn_{11} particles throughout the Zn matrix can readily explain the trend of decreasing biocompatibility with increased Mg content, as seen histologically for the luminally implanted Zn-Mg alloy wires (Figure 13, 14). The increased corrosion resistance imparted by Mg_2Zn_{11} particles (as shown in Figures 11 and 12) can be expected to promote a more aggressive activity of macrophages, as they secrete acids and reactive oxygen species and recruit additional macrophages in an attempt to metabolize the foreign material. This may be considered as a surprising finding since magnesium is widely considered to be a highly biocompatible element in the human body. The formation of intermetallics with unknown biological effects underscores the importance of long term implantation studies of Zn-Mg alloys. It also suggests that Mg concentrations in Zn that are well above what we have evaluated here may result in harmful macrophage responses that undermine the positive remodeling effect imparted by the zinc base metal.

6 Conclusions

In this study, Zn-Mg binary alloys with three ultra-low concentrations of Mg as the alloying element were investigated as potential biodegradable materials for stent applications. The following conclusions were reached:

1. The extruded and drawn Zn-Mg alloys were composed of primary α-Zn and Mg_2Zn_{11} phases. With increasing Mg content from 0.002 to 0.08 wt%, the average grain size of the Zn-Mg alloys decreased from 76 to 6 microns.
2. The yield strength, tensile strength and percent elongation for the Zn-Mg alloys increased with the Mg content increasing from 0.002 wt% to 0.08 wt%. It was observed that increasing Mg content result in finer grains and an increased amount of hard Mg_2Zn_{11} intermetallic phases.
3. The combination of grain boundary strengthening and precipitation strengthening makes the Zn-08Mg alloy stronger and harder among the alloys tested in this study. The Zn-08Mg alloy produced in this study also has favorable ductility with an elongation to fracture value of ~40%,
4. The Zn-08Mg alloy still shows strain-rate sensitivity (significantly reduced TYS at slow rates) and strain softening after yield. These sensitivities need to be addressed for successful vascular design with this material.
5. Biocompatibility was assessed qualitatively from histological images at 1.5, 3, 4.5, 6 and 11 months. The data suggest a slight trend of decreasing biocompatibility with increasing Mg concentration. This may relate to the increased corrosion resistance afforded by the Mg_2Zn_{11} intermetallic phase, which requires a more robust macrophage activity to progressively breakdown the foreign material.

It appears that the Zn-08Mg alloy formulated in this study and then extruded and drawn has corrosion characteristics and biocompatibility that may qualify it as a biodegradable material candidate for vascular stent applications. The mechanical properties, while sufficient in some loading conditions, will require further tuning to eliminate shelf-aging and strain-rate dependent softening.

Acknowledgments

The U.S. National Institute of Health-National Heart, Lung, and Blood Institute (Grant #1R15HL129199-01), U.S. National Institute of Health-National Institute of Biomedical Imaging and Bioengineering (Grant #5R21 EB 019118-02), and National Natural Science Foundation of China (Grant #51401101) are acknowledged for funding this work. Also the China Scholarship Council is acknowledged for a visitor scholar award to Dr. Hualan Jin. PKB was supported by an American Heart Association predoctoral research fellowship administered by the Midwest Division.

The authors thank the staff of the Applied Chemical and Morphological Analysis Laboratory for their assistance with the sample preparation for electron imaging during this work. The authors would like to express appreciation to Jeffrey Brookins for his assistance with scanning electron microscopy imaging of selected specimens and his comments on fractographic analysis. The authors also appreciate valuable comments and suggestions received from Prof. Stephen L. Kampe and Dr. Ehsan Mostaed.

References

1. Fischman DL, Leon MB, Baim DS, Schatz RA, Savage MP, Penn I, et al. A Randomized Comparison of Coronary-Stent Placement and Balloon Angioplasty in the Treatment of Coronary Artery Disease. N Engl J Med. 1994; 331:496–501. [PubMed: 8041414]
2. Elezi S, Kastrati A, Neumann F-J, Hadamitzky M, Dirschinger J, Schömig A. Vessel Size and Long-Term Outcome After Coronary Stent Placement. Circulation. 1998; 98:1875–80. [PubMed: 9799207]
3. Farb A, Weber DK, Kolodgie FD, Burke AP, Virmani R. Morphological Predictors of Restenosis After Coronary Stenting in Humans. Circulation. 2002; 105:2974–80. [PubMed: 12081990]
4. Cook S, Wenaweser P, Togni M, Billinger M, Morger C, Seiler C, et al. Incomplete Stent Apposition and Very Late Stent Thrombosis After Drug-Eluting Stent Implantation. Circulation. 2007; 115:2426–34. [PubMed: 17485593]
5. Chung W-S, Park C-S, Seung K-B, Kim P-J, Lee J-M, Koo B-K, et al. The incidence and clinical impact of stent strut fractures developed after drug-eluting stent implantation. Int J Cardiol. 2008; 125:325–31. [PubMed: 17434616]
6. O'Connell BM, McGloughlin TM, Walsh MT. Factors that affect mass transport from drug eluting stents into the artery wall. Biomed Eng Online. 2010; 9:1–16. [PubMed: 20051137]
7. Kastrati A Md, Schömig A Md, Elezi S Md, Schühlen H Md, Dirschinger J Md, Hadamitzky M Md, et al. Predictive Factors of Restenosis After Coronary Stent Placement. J Am Coll Cardiol. 1997; 30:1428–36. [PubMed: 9362398]
8. Onuma Y, Ormiston J, Serruys PW. Bioresorbable Scaffold Technologies. Circ J. 2011; 75:509–20. [PubMed: 21301138]
9. Waksman R, Pakala R, Kuchulakanti PK, Baffour R, Hellinga D, Seabron R, et al. Safety and efficacy of bioabsorbable magnesium alloy stents in porcine coronary arteries. Catheter Cardiovasc Interv. 2006; 68:607–17. [PubMed: 16969879]
10. Tamai H, Igaki K, Tsuji T, Kyo E, Kosuga K, Kawashima A, et al. A Biodegradable Poly-l-lactic Acid Coronary Stent in the Porcine Coronary Artery. J Interv Cardiol. 1999; 12:443–50.
11. Bünger CM, Grabow N, Sternberg K, Goosmann M, Schmitz K-P, Kreutzer HJ, et al. A Biodegradable Stent Based on Poly(L-Lactide) and Poly(4-Hydroxybutyrate) for Peripheral Vascular Application: Preliminary Experience in the Pig. J Endovasc Ther. 2007; 14:725–33. [PubMed: 17924740]
12. Di Mario C, Griffiths HUW, Goktekin O, Peeters N, Verbist JAN, Bosiers M, et al. Drug-Eluting Bioabsorbable Magnesium Stent. J Interv Cardiol. 2004; 17:391–5. [PubMed: 15546291]

13. Grabow N, Bünger CM, Schultze C, Schmohl K, Martin DP, Williams SF, et al. A Biodegradable Slotted Tube Stent Based on Poly(l-lactide) and Poly(4-hydroxybutyrate) for Rapid Balloon-Expansion. Ann Biomed Eng. 2007; 35:2031–8. [PubMed: 17846893]
14. Bowen PK, Shearier ER, Zhao S, Guillory RJ, Zhao F, Goldman J, et al. Biodegradable Metals for Cardiovascular Stents: from Clinical Concerns to Recent Zn-Alloys. Adv Healthcare Mater. 2016; 5:1121–40.
15. Al-Abdullat Y, Tsutsumi S, Nakajima N, Ohta M, Kuwahara H, Ikeuchi K. Surface Modification of Magnesium by $NaHCO_3$ and Corrosion Behavior in Hank's solution for New Biomaterial Applications. Mater Trans. 2001; 42:1777–80.
16. Erbel R, Di Mario C, Bartunek J, Bonnier J, de Bruyne B, Eberli FR, et al. Temporary scaffolding of coronary arteries with bioabsorbable magnesium stents: a prospective, non-randomised multicentre trial. Lancet. 2007; 369:1869–75. [PubMed: 17544767]
17. Hermawan H, Dubé D, Mantovani D. Degradable metallic biomaterials: Design and development of Fe-Mn alloys for stents. J Biomed Mater Res, Part A. 2010; 93A:1–11.
18. Wang H, Estrin Y, Zúberová Z. Bio-corrosion of a magnesium alloy with different processing histories. Mater Lett. 2008; 62:2476–9.
19. Saris N-EL, Mervaala E, Karppanen H, Khawaja JA, Lewenstam A. Magnesium: An update on physiological, clinical and analytical aspects. Clin Chim Acta. 2000; 294:1–26. [PubMed: 10727669]
20. Moravej M, Mantovani D. Biodegradable Metals for Cardiovascular Stent Application: Interests and New Opportunities. Int J Mol Sci. 2011; 12:4250–70. [PubMed: 21845076]
21. Zhu S, Huang N, Xu L, Zhang Y, Liu H, Sun H, et al. Biocompatibility of pure iron: In vitro assessment of degradation kinetics and cytotoxicity on endothelial cells. Mater Sci Eng: C. 2009; 29:1589–92.
22. Daniels AU, Chang MKO, Andriano KP, Heller J. Mechanical properties of biodegradable polymers and composites proposed for internal fixation of bone. J Appl Biomater. 1990; 1:57–78. [PubMed: 10148987]
23. Seitz JM, Durisin M, Goldman J, Drelich JW. Recent advances in biodegradable metals for medical sutures: A critical review. Adv Healthcare Mater. 2015; 4:1915–36.
24. Peuster M, Hesse C, Schloo T, Fink C, Beerbaum P, von Schnakenburg C. Long-term biocompatibility of a corrodible peripheral iron stent in the porcine descending aorta. Biomaterials. 2006; 27:4955–62. [PubMed: 16765434]
25. Geis-Gerstorfer J, Schille C, Schweizer E, Rupp F, Scheideler L, Reichel HP, et al. Blood triggered corrosion of magnesium alloys. Mater Sci Eng: B. 2011; 176:1761–6.
26. Gu X, Zheng Y, Cheng Y, Zhong S, Xi T. In vitro corrosion and biocompatibility of binary magnesium alloys. Biomaterials. 2009; 30:484–98. [PubMed: 19000636]
27. Liu LJ, Schlesinger M. Corrosion of magnesium and its alloys. Corros Sci. 2009; 51:1733–7.
28. Yang L, Zhang E. Biocorrosion behavior of magnesium alloy in different simulated fluids for biomedical application. Mater Sci Eng: C. 2009; 29:1691–6.
29. Zhang E, Chen H, Shen F. Biocorrosion properties and blood and cell compatibility of pure iron as a biodegradable biomaterial. J Mater Sci: Mater Med. 2010; 21:2151–63. [PubMed: 20396936]
30. Huang T, Cheng J, Bian D, Zheng Y. Fe-Au and Fe-Ag composites as candidates for biodegradable stent materials. JBiomed Mater Res, Part B. 2016; 104:225–40.
31. Lim PN, Lam RN, Zheng YF, Thian ES. Magnesium-calcium/hydroxyapatite (Mg-Ca/HA) composites with enhanced bone differentiation properties for orthopedic applications. Mater Lett. 2016; 172:193–7.
32. He G, Wu Y, Zhang Y, Zhu Y, Liu Y, Li N, et al. Addition of Zn to the ternary Mg-Ca-Sr alloys significantly improves their antibacterial properties. J Mater Chem B. 2015; 3:6676–89. [PubMed: 26693010]
33. Liu Y, Bian D, Wu Y, Li N, Qiu K, Zheng Y, et al. Influence of biocompatible metal ions (Ag, Fe, Y) on the surface chemistry, corrosion behavior and cytocompatibility of Mg-1Ca alloy treated with MEVVA. Colloids Surf, B. 2015; 133:99–107.

34. Willbold E, Gu X, Albert D, Kalla K, Bobe K, Brauneis M, et al. Effect of the addition of low rare earth elements (lanthanum, neodymium, cerium) on the biodegradation and biocompatibility of magnesium. Acta Biomater. 2015; 11:554–62. [PubMed: 25278442]
35. Dorozhkin SV. Calcium orthophosphate coatings on magnesium and its biodegradable alloys. Acta Biomater. 2014; 10:2919–34. [PubMed: 24607420]
36. Chen Y, Zhao S, Liu B, Chen M, Mao J, He H, et al. Corrosion-controlling and osteo-compatible Mg ion-integrated phytic acid (Mg-PA) coating on magnesium substrate for biodegradable implants application. ACS Appl Mater Interfaces. 2014; 6:19531–43. [PubMed: 25363151]
37. Tie D, Feyerabend F, Hort N, Hoeche D, Kainer KU, Willumeit R, et al. In vitro mechanical and corrosion properties of biodegradable Mg Ag alloys. Mater Corros. 2014; 65:569–76.
38. Cheng J, Huang T, Zheng YF. Microstructure, mechanical property, biodegradation behavior, and biocompatibility of biodegradable Fe-Fe_2O_3 composites. J Biomed Mater Res, Part A. 2014; 102:2277–87.
39. Bowen PK, Drelich J, Goldman J. Zinc Exhibits Ideal Physiological Corrosion Behavior for Bioabsorbable Stents. Adv Mater. 2013; 25:2577–82. [PubMed: 23495090]
40. Gong H, Wang K, Strich R, Zhou JG. In vitro biodegradation behavior, mechanical properties, and cytotoxicity of biodegradable Zn Mg alloy. Journal of biomedical materials research Part B, Applied biomaterials. 2015; 103:1632–40.
41. Murni NS, Dambatta MS, Yeap SK, Froemming GRA, Hermawan H. Cytotoxicity evaluation of biodegradable Zn-3Mg alloy toward normal human osteoblast cells. Mater Sci Eng: C. 2015; 49:560–6.
42. Vojtěch D, Kubásek J, Šerák J, Novák P. Mechanical and corrosion properties of newly developed biodegradable Zn-based alloys for bone fixation. Acta Biomater. 2011; 7:3515–22. [PubMed: 21621017]
43. Cheng J, Liu B, Wu YH, Zheng YF. Comparative in vitro Study on Pure Metals (Fe, Mn, Mg, Zn and W) as Biodegradable Metals. J Mater Sci Technol. 2013; 29:619–27.
44. Lastra MD, Pastelin R, Camacho A, Monroy B, Aguilar AE. Zinc intervention on macrophages and lymphocytes response. J Trace Elem Med Biol. 2001; 15:5–10. [PubMed: 11603828]
45. Saltman PD, Strause LG. The role of trace minerals in osteoporosis. J Am Coll Nutr. 1993; 12:384–9. [PubMed: 8409100]
46. Bowen PK, Guillory RJ II, Shearier ER, Seitz J-M, Drelich J, Bocks M, et al. Metallic zinc exhibits optimal biocompatibility for bioabsorbable endovascular stents. Mater Sci Eng: C. 2015; 56:467–72.
47. Wang L, Mostaed E, Cao X, Huang G, Fabrizi A, Bonollo F, et al. Effects of texture and grain size on mechanical properties of AZ80 magnesium alloys at lower temperatures. Mater Des. 2016; 89:1–8.
48. Park SH, Kim S-H, Kim YM, You BS. Improving mechanical properties of extruded Mg-Al alloy with a bimodal grain structure through alloying addition. J Alloys Compd. 2015; 646:932–6.
49. Mani G, Feldman MD, Patel D, Agrawal CM. Coronary stents: A materials perspective. Biomaterials. 2007; 28:1689–710. [PubMed: 17188349]
50. Liu X, Sun J, Yang Y, Pu Z, Zheng Y. In vitro investigation of ultra-pure Zn and its mini-tube as potential bioabsorbable stent material. Mater Lett. 2015; 161:53–6.
51. Li H, Yang H, Zheng Y, Zhou F, Qiu K, Wang X. Design and characterizations of novel biodegradable ternary Zn-based alloys with IIA nutrient alloying elements Mg, Ca and Sr. Mater Des. 2015; 83:95–102.
52. Mostaed E, Sikora-Jasinska M, Mostaed A, Loffredo S, Demir AG, Previtali B, et al. Novel Zn-based alloys for biodegradable stent applications: Design, development and in vitro degradation. J Mech Behav Biomed Mater. 2016; 60:581–602. [PubMed: 27062241]
53. Kubásek J, Vojtěch D, Jablonská E, Pospíšilová I, Lipov J, Ruml T. Structure, mechanical characteristics and in vitro degradation, cytotoxicity, genotoxicity and mutagenicity of novel biodegradable Zn-Mg alloys. Mater Sci Eng: C. 2016; 58:24–35.
54. Shen C, Liu X, Fan B, Lan P, Zhou F, Li X, et al. Mechanical properties, in vitro degradation behavior, hemocompatibility and cytotoxicity evaluation of Zn-1.2Mg alloy for biodegradable implants. RSC Adv. 2016; 6:86410–9.

55. Liu X, Sun J, Qiu K, Yang Y, Pu Z, Li L, et al. Effects of alloying elements (Ca and Sr) on microstructure, mechanical property and in vitro corrosion behavior of biodegradable Zn 1.5Mg alloy. J Alloys Compd. 2016; 664:444–52.
56. Kubásek J, Vojtěch D, Pospíšilová I, Michalcová A, Maixner J. Microstructure and mechanical properties of the micrograined hypoeutectic Zn Mg alloy. Int J Min Met Mater. 2016; 23:1167–76.
57. Dambatta MS, Izman S, Kurniawan D, Farahany S, Yahaya B, Hermawan H. Influence of thermal treatment on microstructure, mechanical and degradation properties of Zn 3Mg alloy as potential biodegradable implant material. Mater Des. 2015; 85:431–7.
58. Lyman, TE. Metallography, Structures and Phase Diagrams. Metals Park, OH 44073: American Society for Metals; 1973. Metals Handbook.
59. Yao C, Wang Z, Tay SL, Zhu T, Gao W. Effects of Mg on microstructure and corrosion properties of Zn-Mg alloy. J Alloys Compd. 2014; 602:101–7.
60. Prosek T, Nazarov A, Bexell U, Thierry D, Serak J. Corrosion mechanism of model zinc magnesium alloys in atmospheric conditions. Corros Sci. 2008; 50:2216–31.
61. Li B, Dong A, Zhu G, Chu S, Qian H, Hu C, et al. Investigation of the corrosion behaviors of continuously hot-dip galvanizing Zn Mg coating. Surf Coat Technol. 2012; 206:3989–99.
62. Wasiur-Rahman S, Medraj M. Critical assessment and thermodynamic modeling of the binary Mg Zn, Ca Zn and ternary Mg Ca Zn systems. Intermetallics. 2009; 17:847–64.
63. Miettinen J. Thermodynamic description of Cu Mg Ni and Cu Mg Zn systems. Calphad. 2008; 32:389–98.
64. Schneider CA, Rasband WS, Eliceiri KW. NIH Image to ImageJ: 25 years of image analysis. Nat Methods. 2012; 9:671–5. [PubMed: 22930834]
65. Bowen PK, Drelich A, Drelich J, Goldman J. Rates of in vivo (arterial) and in vitro biocorrosion for pure magnesium. J Biomed Mater Res, Part A. 2015; 103:341–9.
66. Elliott RP. Constitution of binary alloys. First supplement. 1965:602–3.
67. Atrens, A., ML, Zainal, Abidin NI., Song, G-L. Corrosion of magnesium (Mg) alloys and metallurgical influence. Philadelphia, PA, USA: Woodhead; 2011. Corrosion of magnesium alloys; p. 153
68. Zhang J, Li W, Guo Z. Static recrystallization and grain growth during annealing of an extruded Mg Zn Zr Er magnesium alloy. Journal of Magnesium and Alloys. 2013; 1:31–8.
69. Wang LQ, Ren YP, Sun SN, Zhao H, Li S, Qin GW. Microstructure, Mechanical Properties and Fracture Behavior of As-Extruded Zn Mg Binary Alloys. Acta Metall Sin (Engl Lett). 2017:1–10.
70. Asgharzadeh H, Simchi A, Kim HS. Dynamic restoration and microstructural evolution during hot deformation of a P/M Al6063 alloy. Materials Science and Engineering: A. 2012; 542:56–63.
71. Kayser T, Klusemann B, Lambers HG, Maier HJ, Svendsen B. Characterization of grain microstructure development in the aluminum alloy EN AW-6060 during extrusion. Materials Science and Engineering: A. 2010; 527:6568–73.
72. William, D., Callister, DGR. Materials Science and Engineering: An Introdction. Hoboken NJ: John Wiley and Sons; 2009.
73. Souza RC, Silva ES, Jorge AM Jr, Cabrera JM, Balancin O. Dynamic recovery and dynamic recrystallization competition on a Nb- and N-bearing austenitic stainless steel biomaterial: Influence of strain rate and temperature. Mater Sci Eng: A. 2013; 582:96–107.
74. Yang Q, Deng Z, Zhang Z, Liu Q, Jia Z, Huang G. Effects of strain rate on flow stress behavior and dynamic recrystallization mechanism of Al-Zn-Mg-Cu aluminum alloy during hot deformation. Mater Sci Eng: A. 2016; 662:204–13.
75. Liang ZY, Wang X, Huang W, Huang MX. Strain rate sensitivity and evolution of dislocations and twins in a twinning-induced plasticity steel. Acta Mater. 2015; 88:170–9.
76. Scott C, Remy B, Collet J-L, Cael A, Bao C, Danoix F, et al. Precipitation strengthening in high manganese austenitic TWIP steels. Int J Mater Res. 2011; 102:538–49.
77. Hansen N. Hall Petch relation and boundary strengthening. Scripta Materialia. 2004; 51:801–6.
78. Li HF, Xie XH, Zheng YF, Cong Y, Zhou FY, Qiu KJ, et al. Development of biodegradable Zn-1X binary alloys with nutrient alloying elements Mg, Ca and Sr. Sci Rep. 2015; 5:10719. [PubMed: 26023878]

Author Manuscript

Author Manuscript

Author Manuscript

Highlights

- Minor alloying with Mg additions improves Zn strength
- Novel micro-alloy exceeds benchmark values desirable for vascular scaffolding
- Minor alloying with Mg additions does not compromise Zn biocompatibility
- Micro-alloys showed age-hardening and strain rate sensitivity

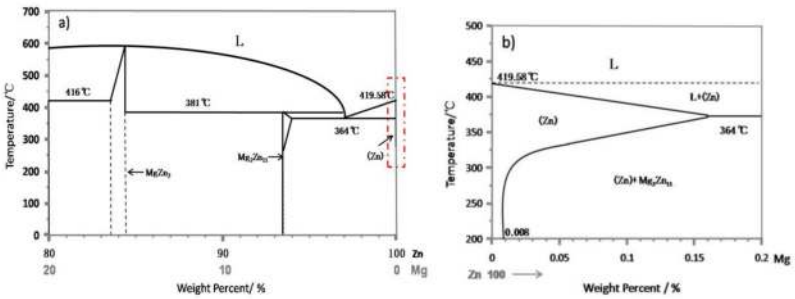

Figure 1.

The Zn-Mg phase diagrams: a) 80 to 100% Zn, b) Mg content from 0 to 0.2% (based on Ref. [66])

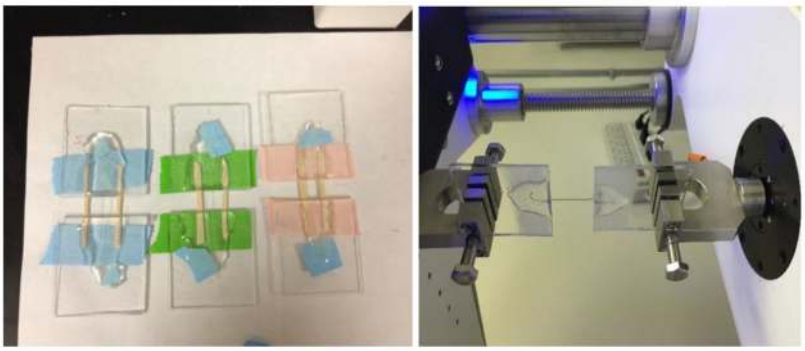

Figure 2.
The wire samples during preparation (a) and tensile testing (b).

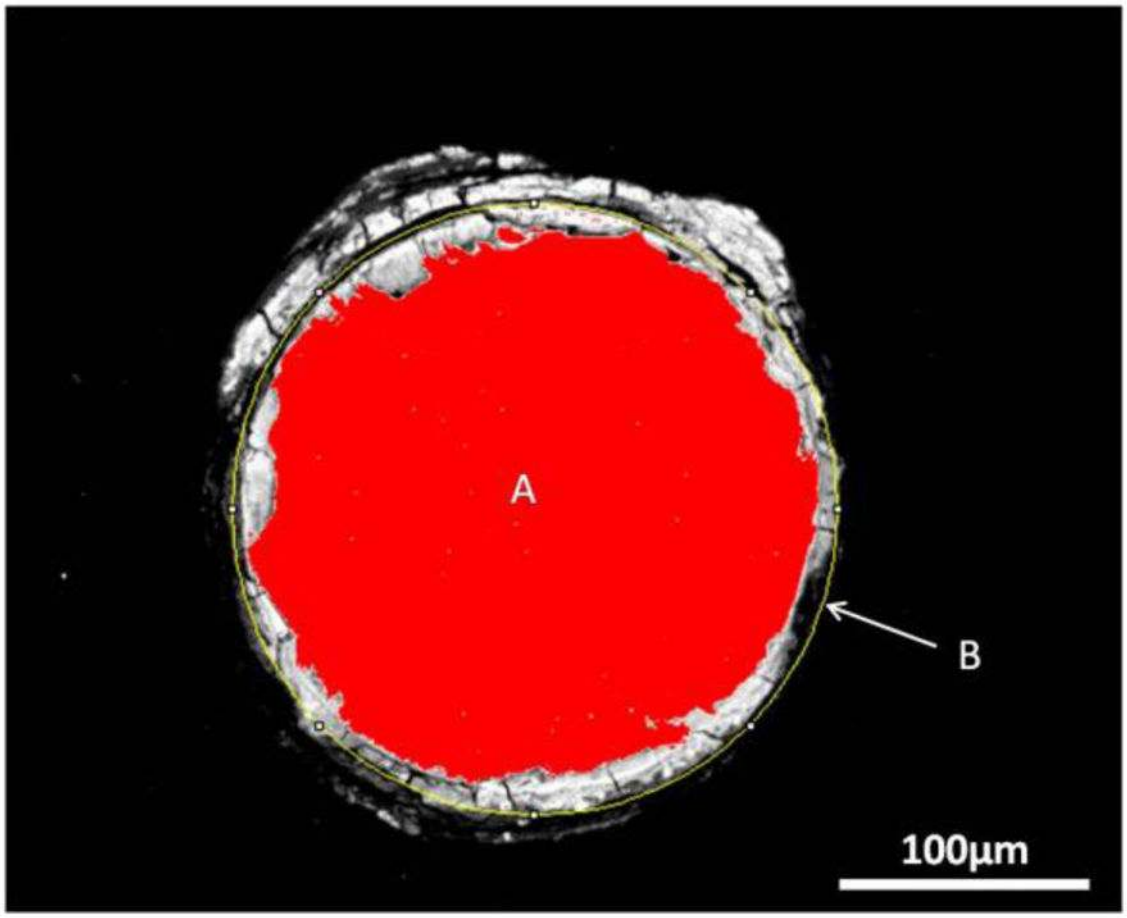

Figure 3.
The ImageJ screen shot for cross sectional analysis. The red area selected by thresholding (area A) is to represent the remaining metallic Zn-Mg alloy, outlined in yellow B.

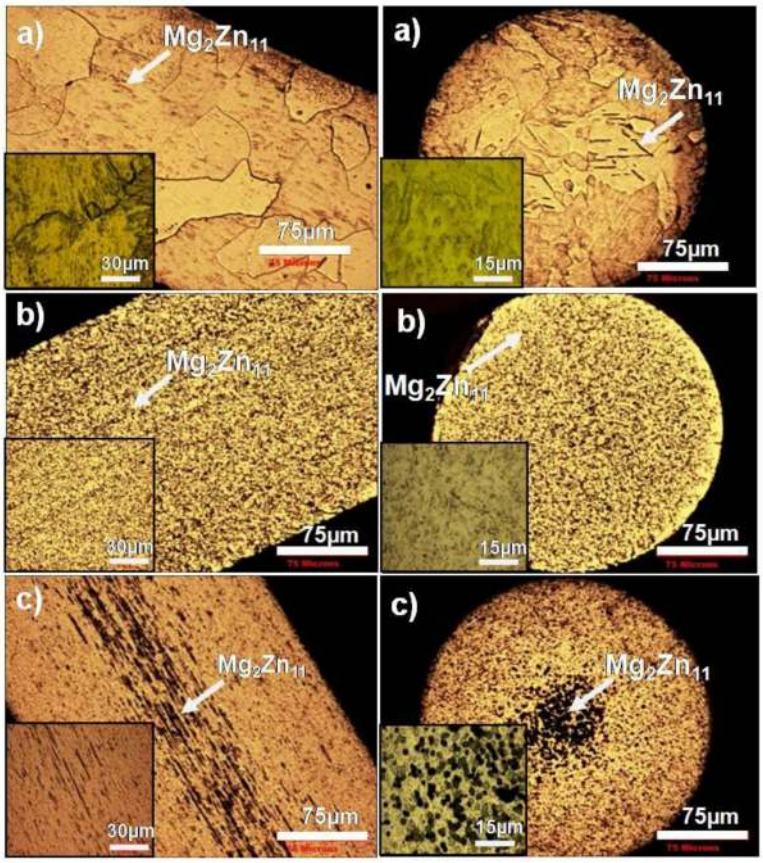

Figure 4.

Microstructure of the investigated samples for longitudinal section and transverse section : (a) Zn-002Mg, (b) Zn-005Mg, (c) Zn-08Mg.

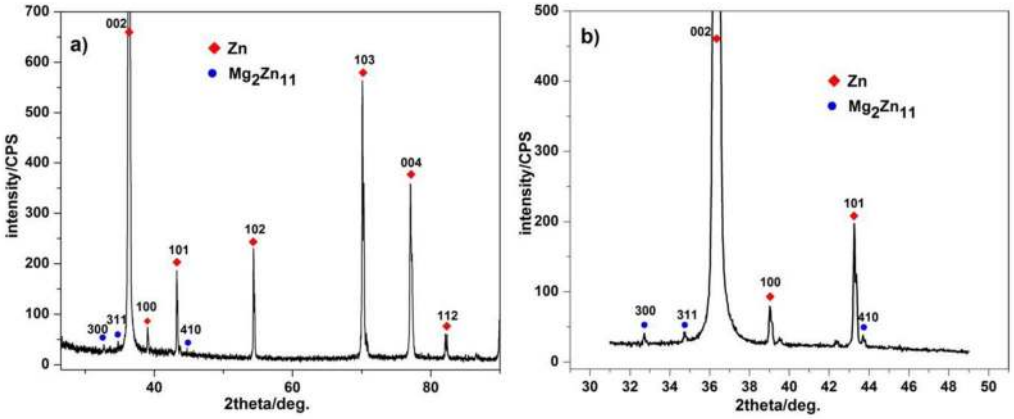

Figure 5.
XRD pattern for the Zn-08Mg sample: a) fast scan; b) slow scan

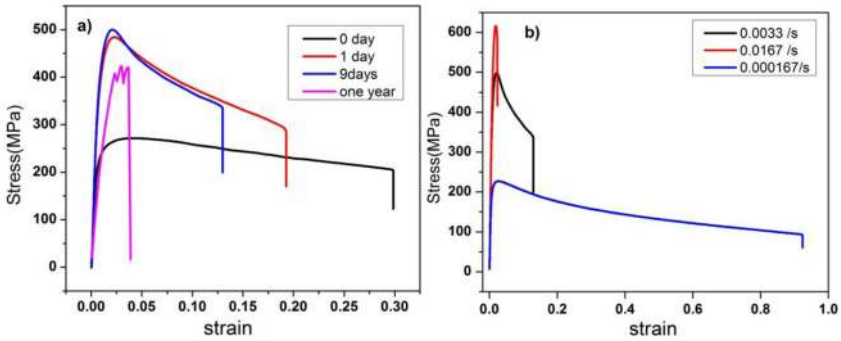

Figure 6.

Representative tensile-stress curve of Zn-08Mg wires: a) different storage time at strain rate of 0.0033/s; b) different strain rates after the wires being stored for 9 days

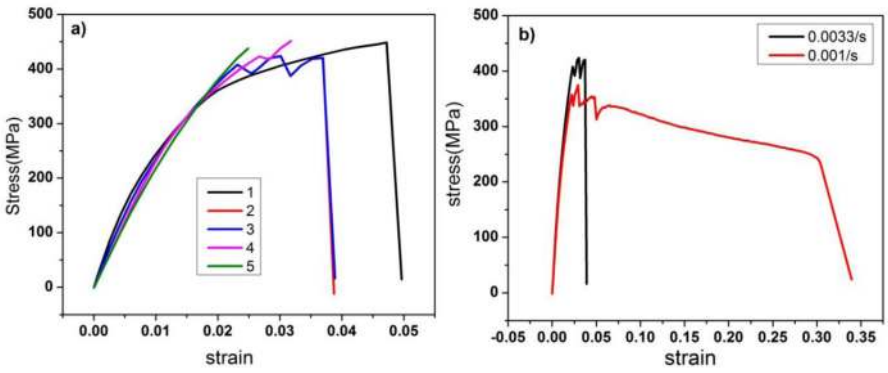

Figure 7.

Representative tensile-stress curve of Zn-08Mg wires: a) five samples at strain rate of 0.0033/s after being stored for a year, b) different strain rate after the wires being stored for a year

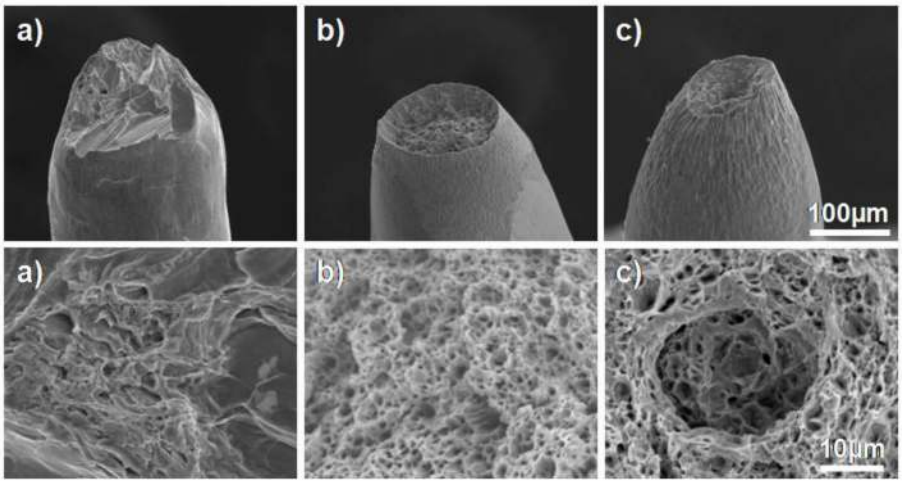

Figure 8.

SEM micrographs of the tensile fracture surfaces: a) Zn-002Mg; b) Zn-005Mg; c) Zn-08Mg (storage half a year, strain rate $1.00\times10^{-3}s^{-1}$).

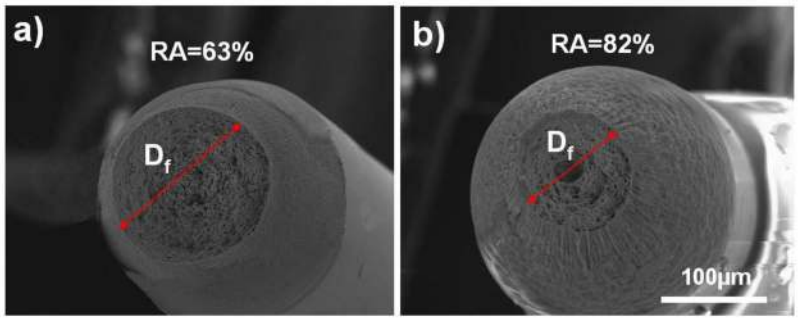

Figure 9.

Reduction in area(%)of the tensile fracture surface for a) Zn-005Mg, and b) Zn-08Mg samples (storage half a year, strain rate $1.00\times10^{-3}s^{-1}$).

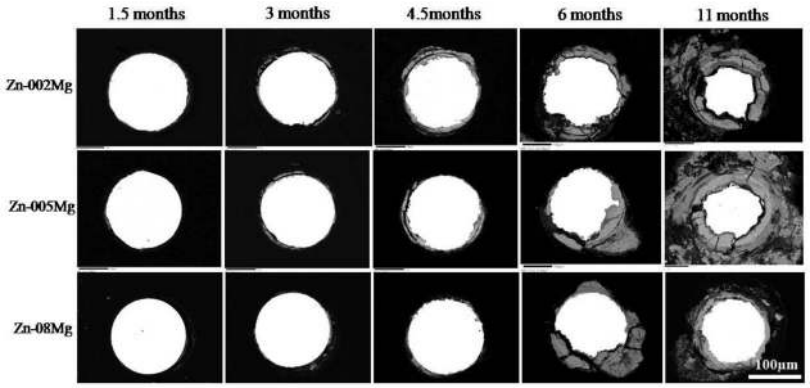

Figure 10.

Representative backscattered electron cross section images from different implantation Zn-Mg wires after 1.5, 3, 4.5, 6 and 11 months' *in vivo*.

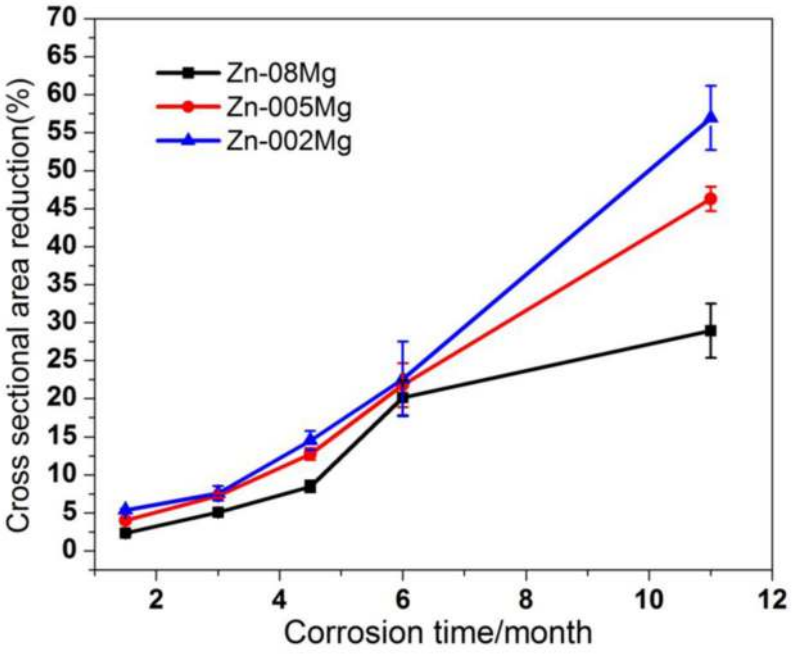

Figure 11.
Measured values for cross sectional area reduction of Zn-Mg explants from *in vivo* study.

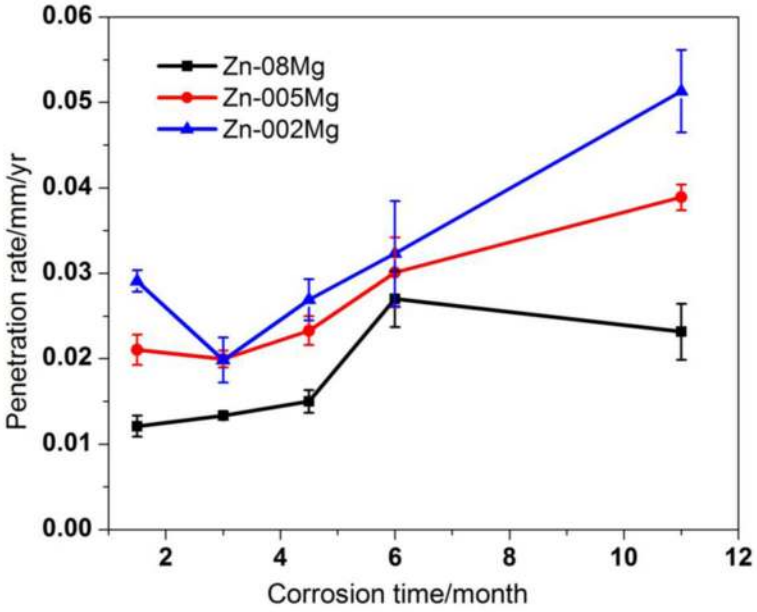

Figure 12.
Penetration rates calculated from the data in Figure 11.

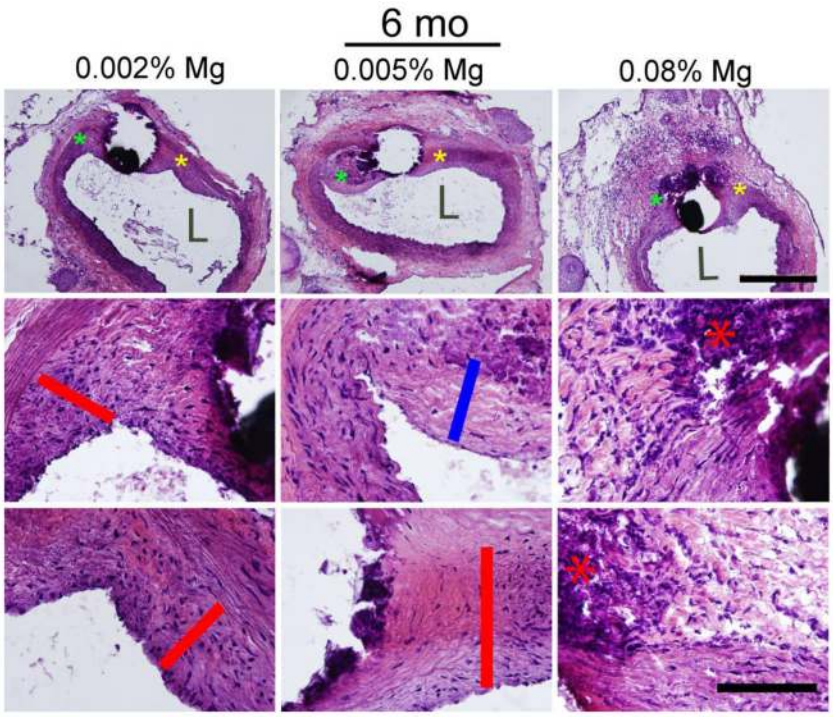

Figure 13.

H&E staining of 6 month implanted Zn-002Mg, Zn-005Mg, and Zn-08Mg wires through the arterial lumen at different magnifications. 2nd and 3rd rows correspond to green and yellow asterisks respectively at high magnifications. L denotes the luminal opening. Scale bars are set to 200 and 100 micrometers.

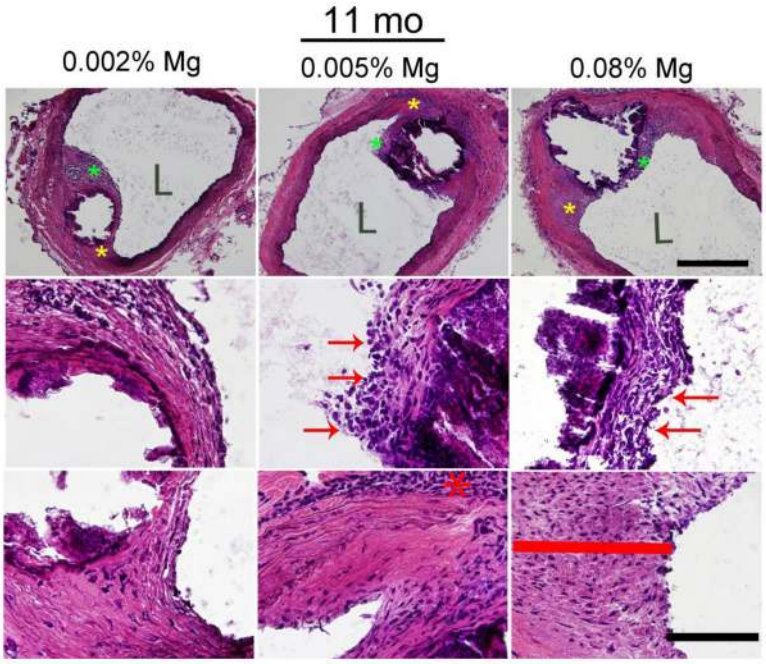

Figure 14.

H&E staining of 11 month implanted Zn-002Mg, Zn-005Mg, and Zn-08Mg wires through the arterial lumen at different magnifications. 2nd and 3rd rows correspond to green and yellow asterisks respectively at high magnifications. L denotes the luminal opening. Scale bars are set to 200 and 100 micrometers.

Table 1

ICP-OES compositional analysis of Zn-Mg wires (wt.%).

Sample	Mg Experimental	Al	Cd	Cu	Fe	Ni	Pb	Zn
	0.002	0.0006	0.00006	0.002	0.0008	0.0001	0.002	Bal.
Zn-Mg	0.005	0.0006	0.00006	0.002	0.0007	0.0001	0.002	Bal
	0.080	0.0007	0.00004	0.002	0.0007	0.0001	0.002	Bal.

Table 2

Average grain size of the investigated samples.

Alloy	Average grain size(μm)
Zn-002Mg	76±10
Zn-005Mg	7.2±1.5
Zn-08Mg	6.3±0.8

Table 3

Mechanical properties of three Mg alloys studied.

Alloy	Shelf time	Strain rate (s^{-1})	Yield strength (MPa)	Tensile strength (MPa)	Ductility %elongation	Hardness (Vickers)
Zn-002Mg(HE)	Half year	1.00×10^{-3}	34±4	63±9	17±3	45±1
Zn-005Mg(HE)	Half year	1.00×10^{-3}	93±1	202±60	28±2	93±1
Zn-08Mg(HE)	Half year	1.00×10^{-3}	221±14	339±42	40±3	103±1
Zn-08Mg(HE)	0 day	3.30×10^{-3}	250	266	29.8	-
Zn-08Mg(HE)	1 day	3.30×10^{-3}	449	483	20	-
Zn-08Mg(HE)	9 days	3.30×10^{-3}	452	498	12.7	-
Zn-08Mg(HE)	9 days	1.67×10^{-4}	216	227	92.3	-
Zn-08Mg(HE)	9 days	1.67×10^{-2}	610	614	2.3	-
Zn-08Mg(HE)	One year	1.00×10^{-3}	337	374	33.9	-
Zn-08Mg(HE)	One year	3.30×10^{-3}	383±6	434±6	3.5±0.5	-

HE: Hot-extrusion

Mater Sci Eng C Mater Biol Appl. Author manuscript; available in PMC 2019 March 01.

Table 4

Mechanical properties of Zn-Mg alloys.

Mg content (Wt. %)	Strain rate (s^{-1})	Yield strength (MPa)	Tensile strength (MPa)	Ductility %elongation	Hardness (Vickers)	Average grain size(μm)	Reference
0.002 (HE)	1.00×10^{-3}	34±4	63±9	17±3	45±1	76±10	Present work
0.005 (HE)	1.00×10^{-3}	93±1	202±60	28±2	93±1	7.2±1.5	Present work
0.02 (extruded at 200°C)	1.00×10^{-3}	132±5	163±8	26±9	–	45	[69]
0.02 (extruded at 300°C)	1.00×10^{-3}	103±5	134±5	6±4	–	117	[69]
0.05 (extruded at 200°C)	1.00×10^{-3}	152±5	232±5	14±2	–	24	[69]
0.05 (extruded at 300°C)	1.00×10^{-3}	122±5	142±5	3±1	–	85	[69]
0.08 (HE)	1.00×10^{-3}	221±14	339±42	40±3	103±1	6.3±0.8	Present work
0.15 (HE)	1.00×10^{-3}	114±8	250±9	22±4	52±5	6.6±0.8	[52]
0.2 (extruded at 200°C)	1.00×10^{-3}	179±5	234±2	8±1	–	16	[69]
0.2 (extruded at 300°C)	1.00×10^{-3}	170±2	205±2	1±1	–	38	[69]
0.5 (extruded at 200°C)	1.00×10^{-3}	227±5	268±5	10±3	–	9	[69]
0.5 (extruded at 300°C)	1.00×10^{-3}	209±5	250±5	1±1	v	14	[69]
0.50 (HE)	1.00×10^{-3}	159±9	297±7	13±1	65±4	4.1±0.4	[52]
0.80 (HE)	2.38×10^{-4}	206±5	301±5	13±3	84±5	–	[53]
1.0 (AC)	4.00×10^{-3}	130±10	180 ± 21	1.8 ±0.2	78 ±3	–	[78]
1.0 (HE)	4.00×10^{-3}	210±15	265±16	8.5±1.0		–	[78]
1.0 (HE)	1.00×10^{-3}	180±7	340±16	6±1	75±4	4.4±0.5	[52]
1.0 (extruded at 200°C)	1.00×10^{-3}	262±10	326±5	5±1	–	9	[69]
1.0 (extruded at 300°C)	1.00×10^{-3}	252±5	317±5	2±1	–	11	[69]
1.0 (HE)	8.33×10^{-3} mm/s *	180±4	252±6	13±2	–	–	[40]
1.2 (AC)	16.7×10^{-3} mm/s *	117±1	130±6	1.4±0.6	93±7	–	[54]
1.5 (AC)	6.67×10^{-4}	120±5	151±13	1.3±0.2	154±23	–	[55]
1.6 (AC)	5.56×10^{-4}	245±12	172±12	–	82±2	35	[56]
1.6 (HE)	5.56×10^{-4}	292±11	365±18	6±2	97±3	9.7	[56]
1.6 (RS-HE)	5.56×10^{-4}	382±11	370±16	9±2	122±3	2.1	[56]

Mg content (Wt. %)	Strain rate (s^{-1})	Yield strength (MPa)	Tensile strength (MPa)	Ductility %elongation	Hardness (Vickers)	Average grain size(μm)	Reference
3.0 (HE)	1.00×10^{-3}	291±9	399±14	1±0.1	117±6	–	[52]
3.0 (AC)	6.67×10^{-4}	–	104±8	2.3±0.30	201±7	–	[57]
3.0 (HO)	6.67×10^{-4}	–	88±1	8.8±0.1	175±8	–	[57]

HE: Hot-extrusion

AC: As-cast

RS-HE: Rapid solidification-hot extrusion

HO: Homogenized

*The references do not include the gauge length of specimens used and therefore, the strain rate has different unit.